COMPARISON OF SHOCK WAVE INTERACTION FOR THE THREE-DIMENSIONAL SUPERSONIC BIPLANE WITH DIFFERENT PLANAR SHAPES

M. Yonezawa*, H. Yamashita*
***Institute of Fluid Science, Tohoku University, 2-1-1 Katahira, Aoba-ku, Sendai, 980-8577, Japan**

Keywords: *Supersonic flow, Supersonic biplane, Shock wave interaction*

Abstract

The supersonic biplane is well known for the airfoil which has zero wave drag at the supersonic speed. However a Mach cone is generated at the wing tip and disturbs the shock wave interaction of the rectangular supersonic biplane with finite span length. The drag increases near the wing tip due to this disturbance. By devising its planar shape, the effect of the wing-tip can be reduced. This paper investigates on the phenomenon of the three-dimensional shock wave interaction for the three-dimensional supersonic biplane with four different kinds of planar shapes using Computational Fluid Dynamics. The drag becomes small when the wing has a small taper ratio, but excessive taper can also lead to more drag than the rectangular wing. When the wing has small sweepback angle and adequate taper ratio, its wing section has better shock wave interaction than that of the two-dimensional supersonic biplane.

Nomenclature

A.o.A:	Angle of attack [deg.]
AR:	Aspect ratio, b/c_{ref}
b:	Span length
c:	Chord length
c_{ref}:	Reference chord length
c_{root}:	Root chord length
c_{tip}:	Tip chord length
C_D:	Drag coefficient
C_p:	Pressure coefficient
h:	Wing clearance
M_∞:	Free-stream Mach number
S:	Reference area, $b \times c_{ref}$
t:	Wing thickness
λ:	Taper ratio, c_{tip}/c_{root}

1 Introduction

Shock waves usually have negative influences on high-speed aircrafts. As seen in the Concorde retired in 2003, the shock waves involve low aerodynamic efficiency and loud noise, which leads to high fare and restrictive areas for supersonic cruising. To realize the next-generation supersonic transport, it is important to create the airplane configuration that can reduce the shock waves, because the strength of the shock wave depends on the aircraft's weight and volume, which are directly related with its configuration.

In 1935, Busemann proposed the concept of supersonic biplane, as illustrated in Fig. 1, for the shock wave reduction [1]. This biplane cancels out the compression waves generated from the leading edges with the expansion waves generated at the vertices by interacting to each other, and thus it can reduce the shock waves greatly. As a result, the biplane achieves low wave drag and low ground noise, compared to a conventional monoplane with the same thickness.

Then, from 1935 to 1960's, other researchers had studied the Busemann's biplane concept furthermore through theoretical discussions and/or wind tunnel experiments. Moeckel and Licher introduced the optimized supersonic biplane configuration having lift in theory [2,3]. Tan calculated the theoretical

values of lift and drag of the supersonic biplane with finite span and rectangular planar shape [4]. Ferri measured the aerodynamic characteristics of the supersonic biplane using the wind tunnel, and compared them with the theoretical characteristics [5].

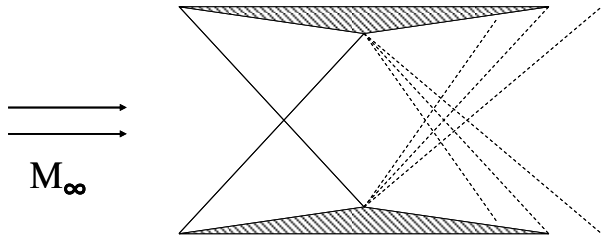

Fig. 1 Supersonic biplane concept

In recent years, Kusunose proposed the use of the supersonic biplane concept for the next-generation supersonic transport. His research group has investigated the concept, based on not only on theory and experiments, but also on the Computational Fluid Dynamics (CFD) simulations [6]. They started with the CFD-based investigation of aerodynamic characteristics for a two-dimensional biplane at both zero-lift and nonzero-lift conditions. Then, they introduced a new configuration of two-dimensional supersonic biplane with improved aerodynamic characteristics using the inverse problem design. Also, they clarified the start/unstart hysteresis phenomenon through the CFD analysis and the wind tunnel experiment, and proposed a configuration-variable mechanism for the two-dimensional supersonic biplane to avoid the unstart phenomenon.

According to Refs. 4 and 6, the supersonic biplane with finite span has a drag penalty because the wing tip generates the Mach cone, which disturbs the ideal shock wave cancellation as illustrated in Fig. 1. For example, Fig. 2 shows the pressure coefficient contour plot on the wing surface and at the symmetry plane for a rectangular supersonic biplane, in which the original biplane airfoil is simply extended in the spanwise direction. This result was obtained through the three-dimensional CFD simulation at the freestream Mach number of 1.7 and the angle of attack of 0 degree, and indicated the Mach cones occurring at the wing tips. Since the Mach cone deflects the flow direction, the region inside the Mach cone has a lower pressure than the shock wave interaction region. It resulted in a high drag penalty, which needs to be reduced. Further studies in Ref. 6 showed that the supersonic biplane wing with a taper and/or a closed wing tip can reduce the drag penalty at the wing tip. Therefore, various tapered wings will be examined in this paper.

This paper discusses the pattern of shock wave interaction and the drag characteristic for a three-dimensional supersonic biplane, by comparing four types of different planar shapes (i.e. trailing-edge-tapered wing, both-edge-tapered wing, leading-edge-tapered wing and caret-type leading-edge-tapered wing) with different taper ratios. This discussion is based on the CFD simulation results: pressure distributions and flow fields of each configuration. Final targets in this study are to find a low-drag biplane configuration, and to clarify a principle for drag reduction in the three-dimensional biplane.

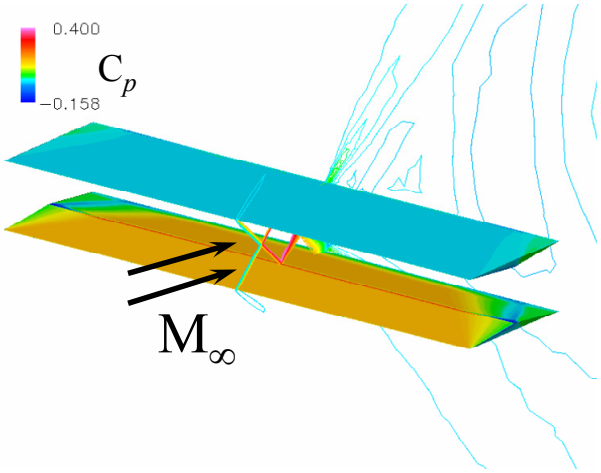

Fig. 2 C_p contour plots on the wing surface and the symmetry plane for the rectangular wing obtained through 3-D CFD simulation (M_∞ = 1.7).

2 Computational methods and conditions

In this research, a three-dimensional unstructured flow solver named TAS (Tohoku university Aerodynamic Simulation) code [7-10] is employed to simulate flow fields around the supersonic biplane. Three-dimensional compressible Euler equations are solved by a

finite-volume cell-vertex scheme. The numerical fluxes are computed using the approximate Riemann solver of Harten-Lax-van Leer-Einfeldt-Wada (HLLEW) [11]. The second order spatial accuracy is realized by a linear reconstruction of the primitive gas dynamic variables with Venkatakrishnan's limiter. The lower/upper symmetric Gauss-Seidel (LU-SGS) implicit method for unstructured mesh [12] is used for the time integration. Figure 3 shows the unstructured mesh for the present flow solver. This research simulates the flow fields only for a half wing, which does not have cross flows at the root section, to reduce the computational time. All mesh points sum up to about 2 million. As seen in Fig. 3, enough grid points are placed between two wings to capture the shock wave interaction. All configurations are analyzed at the angle of attack of 0 degree and a freestream Mach number of 1.7.

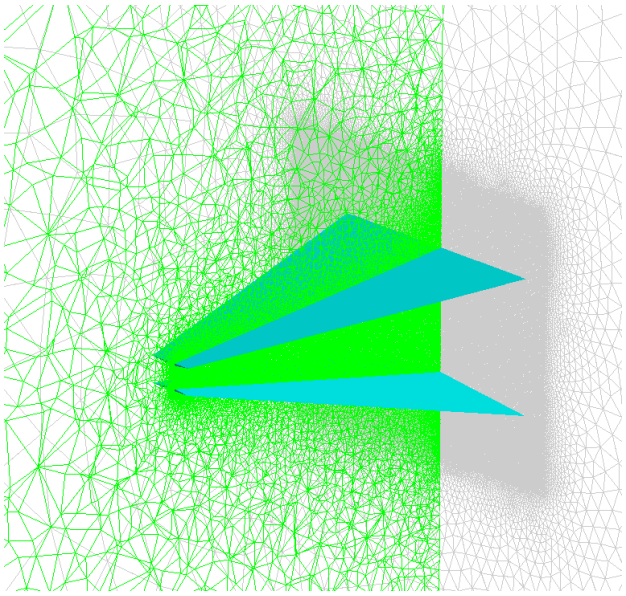

Fig. 3 3-D unstructured grid (e.g. for both-edge-tapered wing).

3 Geometry definitions

Figures 4-7 illustrates four different types of three-dimensional biplane configurations to be considered in this study. These have different planar shapes: trailing-edge-tapered wing, both-edge-tapered (leading and trailing-edge-tapered) wing, leading-edge-tapered wing and caret-type leading-edge-tapered wing. Each configuration has the same reference area ($S = b \times c_{ref} = 4$) and the same aspect ratio ($AR = b/c_{ref} = 4$). These wings have a similar geometry of cross-section parallel to the freestream, as illustrated in Fig. 8, at any span section. This is composed of two isosceles triangular airfoils with thickness to chord ratio (t/c) of 0.05. At the freestream Mach number of 1.7, the generated two-dimensional oblique shock wave's angle (β) from the leading edges is 41.82 degrees. The clearance of the biplane (h/c) is set to 0.5054 by considering the shock wave diffraction involved in the shock wave interaction.

The trailing-edge-tapered wing (TTW) shown in Fig. 4 has a quadrilateral planar shape tapered at the trailing edge, and the leading edge is perpendicular to the freestream. The taper ratio of the trailing-edge-tapered wing is set to 0, 0.2, 0.4, 0.5, 0.6, 0.8 and 1.0, and is identified by the number following the biplane configuration. For example, TTWt06 refers to the trailing-edge-tapered wing with a taper ratio of 0.6. The same nomenclature is valid for the taper ratio in the other configurations.

The both-edge-tapered wing (BTW) shown in Fig. 5 has a quadrilateral planar shape tapered at both the leading and trailing edges, so that the line connecting the vertices at each wing span section is perpendicular to the freestream. The taper ratio of the both-edge-tapered wing is set to 0, 0.1, 0.2, 0.3, 0.4, 0.5, 0.6 and 1.0.

The leading-edge-tapered wing (LTW) shown in Fig. 6 has a quadrilateral planar shape tapered at the leading edge, and the trailing edge is perpendicular to the freestream. The taper ratio of the leading-edge-tapered wing is set to 0.2, 0.4, 0.5, 0.6 and 1.0.

The caret-type leading-edge-tapered wing (CTW) shown in Fig. 7 has a quadrilateral planar shape tapered at both the leading and trailing edge, so that the angle of the leading edge from a side view is the same as the angle of the two-dimensional oblique shock wave. The taper ratio of the caret-type leading-edge-tapered wing is set to 0, 0.2, 0.4, 0.5, 0.6, 0.8 and 1.0. The wing configuration in front of the vertex is equivalent to a caret wing, which does not generate cross flow behind the shock wave i.e. planar shock front under the wing surface in theory.

These four types of three-dimensional biplane configurations match the rectangular wing configuration (RW) when the taper ratio is set to 1.0. Upper and lower wings of all the configurations are symmetric about the plane at half the wing clearance, therefore all the configurations do not have lift at the angle of attack of 0 degree. In addition, the monoplane of each configuration is also analyzed to compare the pressure distributions with and without the shock wave interaction.

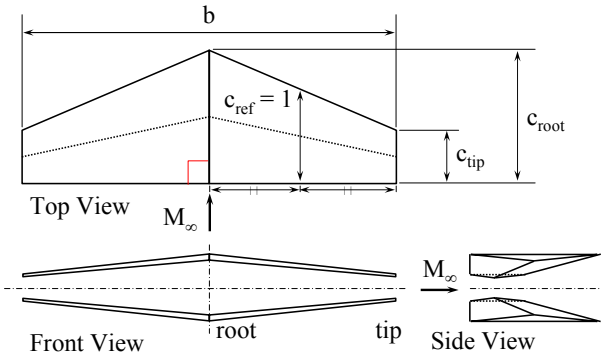

Fig. 4 Geometry of the trailing-edge-tapered wing.

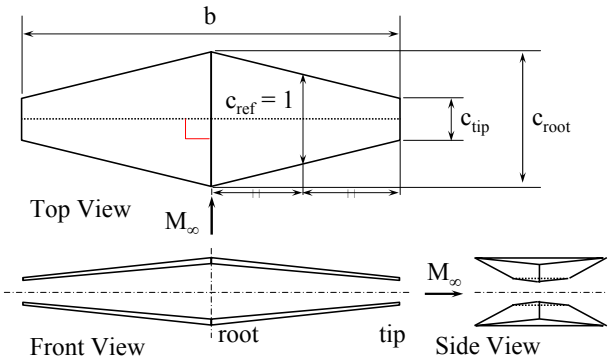

Fig. 5 Geometry of the both-edge-tapered wing.

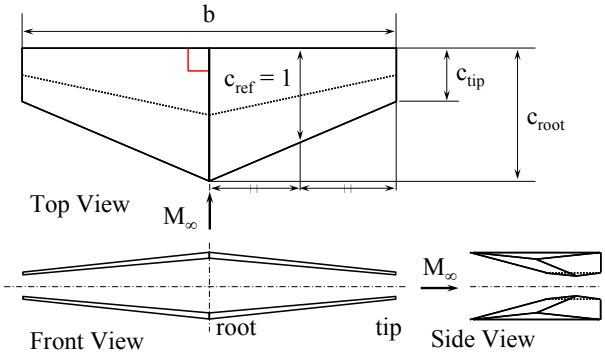

Fig. 6 Geometry of the leading-edge-tapered wing.

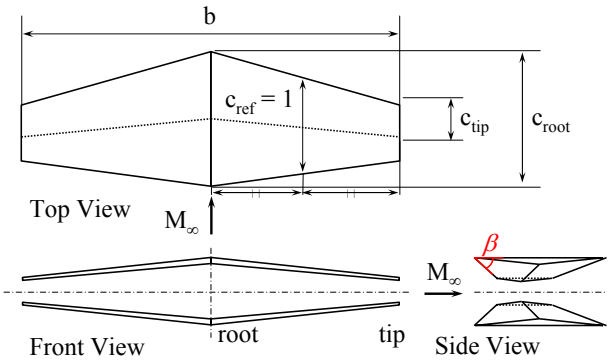

Fig. 7 Geometry of the caret-type leading-edge-tapered wing.

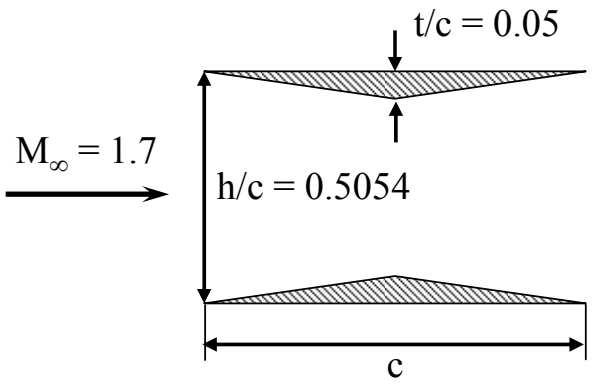

Fig. 8 Geometry of the wing cross-section.

4 Results and discussion

4.1 Comparison of the drag coefficients

The drag coefficients of the four types of three-dimensional biplane configurations with different taper ratios were compared as shown in Fig. 9. The results indicated the both-edge-tapered wing with the taper ratio of 0.2 (BTWt02) has minimum drag.

The drag of the trailing-edge-tapered wing decreases as the taper ratio decreases from the rectangular wing configuration where the taper ratio is one (RW to TTWt04). However, when the taper ratio becomes smaller than 0.4, the drag starts to increase rapidly and it surpasses the drag of the rectangular wing (TTWt04 to TTWt00).

The drag of the leading-edge-tapered wing showed a similar trend to the trailing-edge-tapered wing but it diverged more rapidly. The drag decreases from the rectangular value until

the taper ratio becomes 0.6 (RW to LTWt06), and then increases when the taper ratio is smaller than 0.6 (LTWt06 to LTWt02).

The drags of the both-edge-tapered wing and the caret-type leading-edge-tapered wing become smaller than that of the rectangular wing when the taper ratio is around 0.2. The both-edge-tapered wing with the taper ratio of 0.2 (BTWt02) presented the smallest drag among all the configurations.

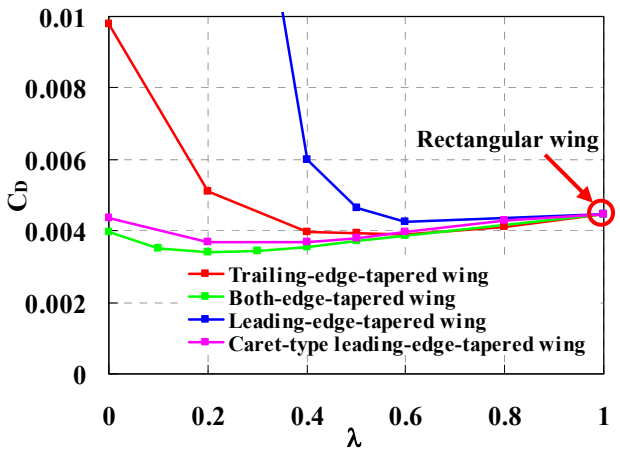

Fig. 9 Comparison of drag coefficients for four biplane configurations with different taper ratios (M_∞ = 1.7, A.o.A. = 0 deg.).

4.2 Investigation of each shock wave interaction

In order to take a more detailed look at the shock wave interaction of each configuration, C_p contour plots on the inside wing surface for the four types of configurations with a taper ratio of 0, 0.2, 0.4, 0.6 and 1 (rectangular wing) are shown in Fig. 10.

The regions influenced by the Mach cones near the wing tips were reduced from those of the rectangular wing when the wing had a smaller taper ratio irrespective of the planar shapes. Next, each planar shape is discussed in detail.

The trailing-edge-tapered wing:

The region near the wing root had higher pressure, compared to the other regions where the shock waves interacted ideally, and the oblique shock wave from the leading edge at the root section reflected in front of the triangle vertex located at half the chord length. This phenomenon became more prominent when the wing had a smaller taper ratio (TTWt06 to TTWt00). As a result, the reflected shock wave hit on the wing surface in front of the trailing edge and thus the shock wave interaction was disturbed near the wing root.

The both-edge-tapered wing:

The Mach cone was generated at the wing root and slightly disturbed the shock wave interaction. The Mach cone from the leading edge at the root section reflected behind the vertex of the triangle. However, the pressure behind the vertices was higher than the pressure in front of the vertices at the mid-span section (BTWt06 to BTWt00).

The leading-edge-tapered wing:

This configuration generated the Mach cone at the wing root, which influenced a larger region than the both-edge-tapered wing. This influence extended for over a half of the wing. The location where the oblique shock wave from the leading edge reflected moved forward and the reflected shock wave became stronger when the wing had a smaller taper ratio (LTWt06 to LTWt02). As a result, a choked flow occurs near the wing tip (LTWt02).

The caret-type leading-edge-tapered wing:

The two-dimensionality of the flow field is kept from the leading edge to the vertex at the wing root (CTWt00 - CTWt06). The Mach cone was generated behind the vertex at the wing root.

Type \ λ	0	0.2	0.4	0.6	1.0
Trailing-edge-tapered wing	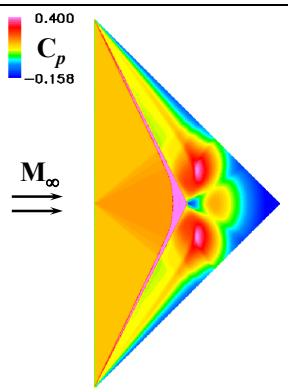 TTWt00	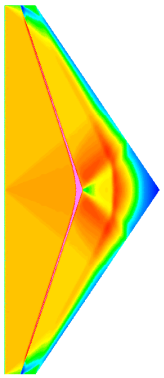 TTWt02	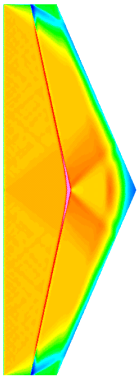 TTWt04	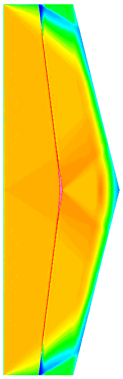 TTWt06	 RW
Both-edge-tapered wing	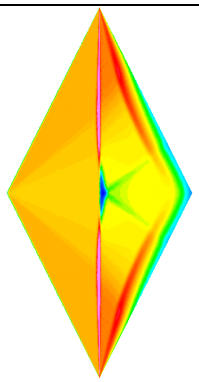 BTWt00	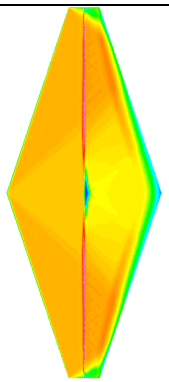 BTWt02	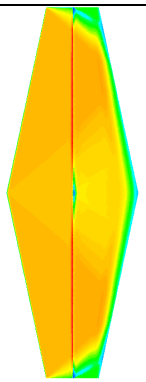 BTWt04	 BTWt06	 RW
Leading-edge-tapered wing		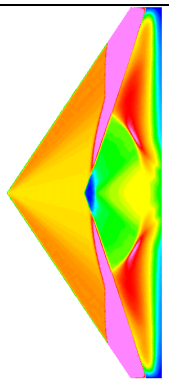 LTWt02	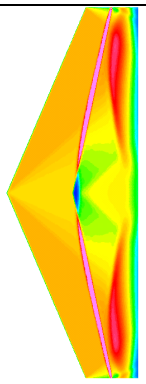 LTWt04	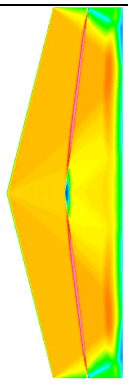 LTWt06	 RW
Caret-type leading-edge-tapered wing	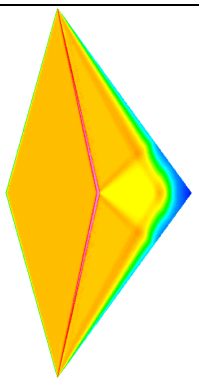 CTWt00	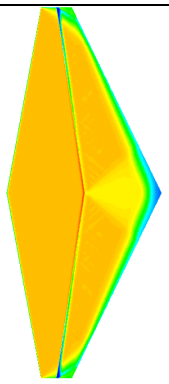 CTWt02	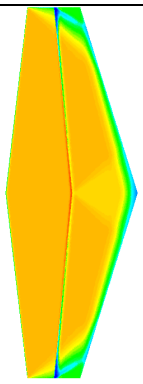 CTWt04	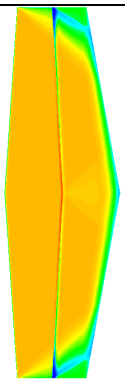 CTWt06	 RW

Fig. 10 C_p contour plots on the wing surfaces (shock wave interaction side) of four biplane configurations with different taper ratios (M_∞ = 1.7, A.o.A. = 0 deg.).

4.3 Comparison of the pressure on the wing surface

In the previous section, the shock wave interaction patterns of all the configurations were examined. This section compares the pressure distributions at the mid-span section where the flow fields were not affected by the Mach cones and the shock wave interaction succeeded. The chordwise pressure coefficient distributions on the wing surfaces of each configuration at the wing section of b/c_{ref} = 1 are shown in Figs. 11-14.

In the trailing-edge-tapered wing shown in Fig. 11, the strength of the pressure coefficient in front of the vertex became slightly smaller and that behind the vertex became smaller when the wing had a smaller taper ratio. At this section, the drag increased as compared to the rectangular wing.

In the both-edge-tapered wing shown in Fig. 12 and the leading-edge-tapered wing shown in Fig. 13, the strength of the pressure coefficients in front of the vertex became larger and behind the vertex also became larger when the wing had a smaller taper ratio. At this time, strength of the pressure coefficient behind the vertex became larger than in front of the vertex. The drags decreased as compared to the rectangular wing.

In the caret-type leading-edge-tapered wing shown in Fig. 14, the strength of the pressure coefficient in front of the vertex stayed constant and behind the vertex became a little smaller when the wing had a smaller taper ratio. The drag was nearly equal to that of the rectangular wing.

Summarizing from sweepback angle perspective, the strength of the pressure coefficient in front of the vertex of the caret-type leading-edge-tapered wing is identical to the strength of the rectangular wing. The strength of the pressure coefficient in front of the vertex of the configuration which has a smaller sweepback angle than the sweepback angle of the caret-type leading-edge-tapered wing, like the trailing-edge-tapered wing, became smaller when the wing has a smaller taper ratio. On the other hand, when the configuration has a larger sweepback angle than the sweepback angle of the caret-type leading-edge-tapered wing, like the both-edge-tapered wing and the leading-edge-tapered wing, the strength of the pressure coefficient in front of the vertex became larger if the wing has a smaller taper ratio.

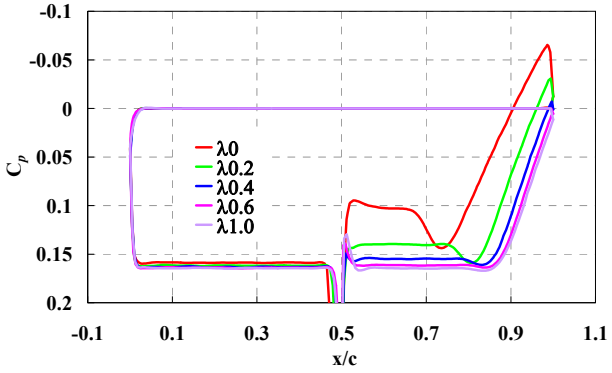

Fig. 11 Chordwise C_p distributions on the surfaces of trailing-edge-tapered wings with different taper ratios at the section of b/c_{ref} of 1 (M_∞ = 1.7, A.o.A. = 0 deg.).

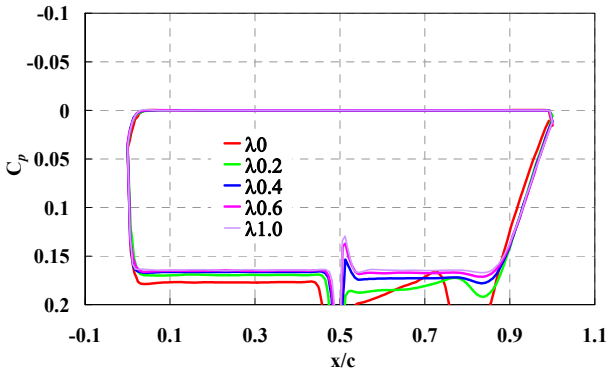

Fig. 12 Chordwise C_p distributions on the surfaces of both-edge-tapered wings with different taper ratios at the section of b/c_{ref} of 1 (M_∞ = 1.7, A.o.A. = 0 deg.).

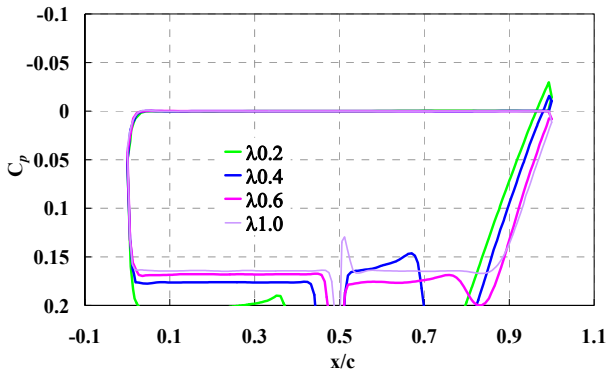

Fig. 13 Chordwise C_p distributions on the surfaces of leading-edge-tapered wings with different taper ratios at the section of b/c_{ref} of 1 (M_∞ = 1.7, A.o.A. = 0 deg.).

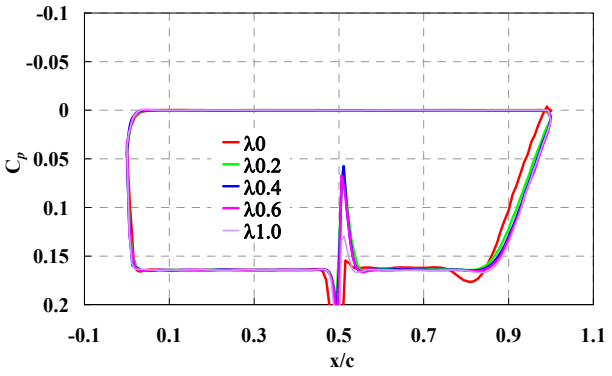

Fig. 14 Chordwise C_p distributions on the surfaces of caret-type leading-edge-tapered wings with different taper ratios at the section of b/c_{ref} of 1 (M_∞ = 1.7, A.o.A. = 0 deg.).

4.4 Comparison of the pressure distribution on the wing surface of the single wing

The pressure difference on the wing surface between the region in front of the vertex and the region behind the vertex was discussed in the previous section. In this section, the cause of the difference in pressure on the wing surface is analyzed by running CFD simulations using only a single wing of each biplane configuration. The chordwise pressure coefficient distributions on the wing surfaces of each single wing configuration at the wing section of b/c_{ref} = 1 are shown in Figs. 15-18.

The strength of the pressure coefficient in front of the vertex of the single wing and the biplane were identical in all configurations. However, behind the vertex, a different behavior was observed.

In the case of the single wing of the trailing-edge-tapered wing shown in Fig. 15, the pressure became smaller for smaller taper ratios. As a result, the pressure behind the vertex of the biplane of the trailing-edge-tapered wing also became smaller.

In the single wing of the both-edge-tapered wing shown in Fig. 16, the pressure coefficient behind the vertex stayed nearly constant, even though the pressure in front of the vertex increased. As a result, the biplane's pressure behind the vertex became larger.

In the single wing of the leading-edge-tapered wing shown in Fig. 17, the pressure coefficient behind the vertex became smaller for smaller taper ratios, as in the case of the trailing-edge-tapered wing. However, in this case, the pressure increased in front of the vertex, unlike the trailing-edge-tapered wing. As a result, the biplane's pressure behind the vertex became larger.

In the single wing of the caret-type leading-edge-tapered wing shown in Fig. 18, the pressure coefficient behind the vertex stayed constant. As a result, the biplane's pressure behind the vertex stayed nearly constant too. This is because the direction of the shock wave from the leading edge was deflected by the difference in pressure.

Summarizing from sweepback angle perspective, the strength of the pressure coefficient behind the vertex of the caret-type leading-edge-tapered wing and the both-edge-tapered wing is nearly equal to the strength of the rectangular wing. On the other hand, the strength of the pressure coefficient behind the vertex became smaller when they have a smaller taper ratio with some configurations. Such configurations are those in which the line connecting the vertices of each wing section has high forward sweep angle or sweepback angle like the trailing-edge-tapered wing and the leading-edge-tapered wing.

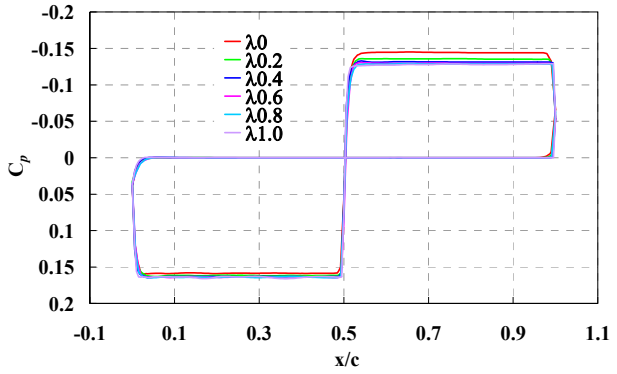

Fig. 15 Chordwise C_p distributions on the surfaces of trailing-edge-tapered single wings with different taper ratios at the section of b/c_{ref} of 1 (M_∞ = 1.7, A.o.A. = 0 deg.).

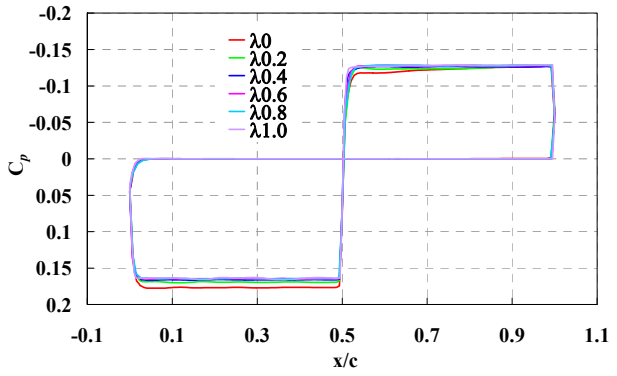

Fig. 16 Chordwise C_p distributions on the surfaces of both-edge-tapered single wings with different taper ratios at the section of b/c_{ref} of 1 (M_∞ = 1.7, A.o.A. = 0 deg.).

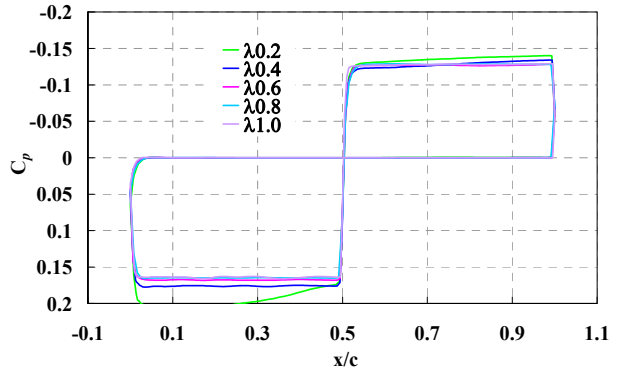

Fig. 17 Chordwise C_p distributions on the surfaces of leading-edge-tapered single wings with different taper ratios at the section of b/c_{ref} of 1 (M_∞ = 1.7, A.o.A. = 0 deg.).

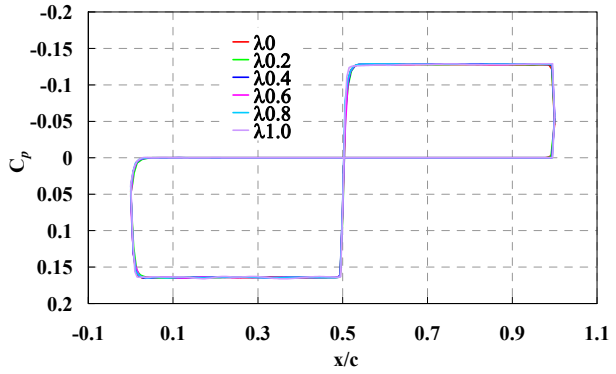

Fig. 18 Chordwise C_p distributions on the surfaces of caret-type leading-edge-tapered single wings with different taper ratios at the section of b/c_{ref} of 1 (M_∞ = 1.7, A.o.A. = 0 deg.).

5 Conclusion

This paper compared the shock wave interaction and the drag of three-dimensional supersonic biplane with four different types of planar shapes and taper ratios through the CFD simulations. As a result, the following conclusions regarding the geometry definition of the supersonic biplane can be made.

The pressure coefficient in front of the vertex becomes larger when the wing has high sweepback angle.

The pressure coefficient behind the vertex becomes nearly equal to that of the rectangular wing when the line connecting the vertices of each wing section is roughly perpendicular to the freestream.

Because of these considerations, the low drag tapered wing configuration has a small sweepback angle and a large taper ratio so that the line connecting the vertices of each wing section is nearly perpendicular to the freestream.

References

[1] Liepmann H W and Roshko A. *Elements of gas dynamics*. John Wiley & Sons Inc., New York, pp 109-123, 1957.

[2] Moeckel W E. Theoretical aerodynamic coefficients of the two-dimensional supersonic biplane. NACA T.N. No. 1316, 1947.

[3] Licher R M. Optimum two-dimensional multiplanes in supersonic flow. Report No. SM-18688, Douglass Aircraft Co., 1955.

[4] Tan H S. The aerodynamics of supersonic biplanes of finite span. WADC TECHNICAL REPORT 52-276, 1950.

[5] Ferri A. *Elements of aerodynamics of supersonic flow*. The Macmillan Company, New York, pp 154-160, 1949 (Also published from Dover Phoenix Edition, Dover Publications, Inc., New York, 2005).

[6] Kusunose K et al. *Aerodynamic design of supersonic biplane: cutting edge and related topics*. Tohoku University Press, Sendai, 2007.

[7] Ito Y and Nakahashi K. Direct surface triangulation using stereolithography data. *AIAA Journal*, Vol. 40, No. 3, pp 490-496, March 2002.

[8] Ito Y and Nakahashi K. Surface triangulation for polygonal models based on CAD data. *International Journal for Numerical Methods in Fluids*, Vol. 39, Issue 1, pp 75-96, May 2002.

[9] Sharov D and Nakahashi K. A boundary recovery algorithm for delaunay tetrahedral meshing. *Proceedings of the 5th International Conference on Numerical Grid Generation in Computational Field Simulations*, pp 229-238, 1996.

[10] Nakahashi K, Ito Y and Togashi F. Some challenge of realistic flow simulations by unstructured grid CFD. *International Journal for Numerical Methods in Fluids*, Vol. 43, pp 769-783, 2003.

[11] Obayashi S and Guruswamy G P. Convergence acceleration of a Navier-Stokes solver for efficient static aeroelastic computations. *AIAA Journal*, Vol. 33, No. 6, pp 1134-1141, 1995.

[12] Sharov D and Nakahashi K. Reordering of hybrid unstructured grids for lower-upper symmetric Gauss-Seidel computations. *AIAA Journal*, Vol. 36, No. 3, pp 484-486, 1998.

Copyright Statement

The authors confirm that they, and/or their company or institution, hold copyright on all of the original material included in their paper. They also confirm they have obtained permission, from the copyright holder of any third party material included in their paper, to publish it as part of their paper. The authors grant full permission for the publication and distribution of their paper as part of the ICAS2008 proceedings or as individual off-prints from the proceedings.